Journal of Catalysis 286 (2012) 287–297

Contents lists available at SciVerse ScienceDirect

Journal of Catalysis

journal homepage: www.elsevier.com/locate/jcat

Performance, structure, and mechanism of CeO_2 in HCl oxidation to Cl_2

Amol P. Amrute [a], Cecilia Mondelli [a], Maximilian Moser [a], Gerard Novell-Leruth [b], Núria López [b], Dirk Rosenthal [c], Ramzi Farra [c], Manfred E. Schuster [c], Detre Teschner [c,d], Timm Schmidt [e], Javier Pérez-Ramírez [a,*]

[a] Institute for Chemical and Bioengineering, Department of Chemistry and Applied Biosciences, ETH Zurich, Wolfgang-Pauli-Strasse 10, CH-8093 Zurich, Switzerland
[b] Institute of Chemical Research of Catalonia (ICIQ), Av. Països Catalans 16, 43007 Tarragona, Spain
[c] Fritz-Haber Institute of the Max Planck Society, D-14159 Berlin, Germany
[d] Institute of Isotopes, Hungarian Academy of Science, H-1525 Budapest, Hungary
[e] Bayer MaterialScience AG, PUR-PTI-PRI, Chempark B598, D-41538 Dormagen, Germany

ARTICLE INFO

Article history:
Received 9 August 2011
Revised 20 November 2011
Accepted 22 November 2011
Available online 26 December 2011

Keywords:
Chlorine recycling
HCl oxidation
CeO_2
Oxygen vacancies
Chlorination

ABSTRACT

Experimental and theoretical studies reveal performance descriptors and provide molecular-level understanding of HCl oxidation over CeO_2. Steady-state kinetics and characterization indicate that CeO_2 attains a significant activity level, which is associated with the presence of oxygen vacancies. Calcination of CeO_2 at 1173 K prior to reaction maximizes both the number of vacancies and the structural stability of the catalyst. X-ray diffraction and electron microscopy of samples exposed to reaction feeds with different O_2/HCl ratios provide evidence that CeO_2 does not suffer from bulk chlorination in O_2-rich feeds (O_2/HCl $\geqslant$ 0.75), while it does form chlorinated phases in stoichiometric or sub-stoichiometric feeds (O_2/HCl $\leqslant$ 0.25). Quantitative analysis of the chlorine uptake by thermogravimetry and X-ray photoelectron spectroscopy indicates that chlorination under O_2-rich conditions is limited to few surface and subsurface layers of CeO_2 particles, in line with the high energy computed for the transfer of Cl from surface to subsurface positions. Exposure of chlorinated samples to a Deacon mixture with excess oxygen rapidly restores the original activity levels, highlighting the dynamic response of CeO_2 outermost layers to feeds of different composition. Density functional theory simulations reveal that Cl activation from vacancy positions to surface Ce atoms is the most energy-demanding step, although chlorine–oxygen competition for the available active sites may render re-oxidation as the rate-determining step. The substantial and remarkably stable Cl_2 production and the lower cost of CeO_2 make it an attractive alternative to RuO_2 for catalytic chlorine recycling in industry.

1. Introduction

The heterogeneously catalyzed gas-phase oxidation of HCl to Cl_2 (Eq. (1)) is a sustainable route to recycle chlorine from by-product HCl streams derived from the manufacture of polyurethanes and polycarbonates with low energy input [1,2]. The amount of waste HCl raises due to the growing demand for these versatile plastics. As selling the HCl excess is unfeasible, and the neutralization option is unattractive, its catalytic conversion to Cl_2 is receiving an increasing interest.

$$4HCl + O_2 \leftrightarrow 2Cl_2 + 2H_2O \quad (1)$$

Since its introduction and till recent times, the industrialization of HCl oxidation has suffered from many failed attempts to obtain sufficiently active and durable catalysts. The $CuCl_2$/pumice catalyst patented by Henry Deacon in 1868 [3] exhibited fast deactivation due to volatilization of the active phase in the form of copper chlorides. Other examples of processes of limited success are the Shell-Chlor process (based on $CuCl_2$–KCl/SiO_2) [4] and the Mitsui-Toatsu process (based on Cr_2O_3/SiO_2) [5]. Only recently, ruthenium supported on specific carriers was successfully developed for large-scale chlorine recycling [1]. In particular, Sumitomo has applied RuO_2/SiO_2/TiO_2-rutile in a plant producing 100 kton Cl_2 per year [2,6], while Bayer's RuO_2/SnO_2–Al_2O_3 catalyst [7,8] has been piloted and is ready for industrial use. The distinctive features of RuO_2-based catalysts are the high activity at low temperature and the remarkable stability against bulk chlorination [9–11].

The implementation of the catalytic HCl oxidation technology would expand if cheaper, but comparably stable, alternatives to RuO_2-based catalysts were developed. The high and fluctuating market price of ruthenium indeed reflects in large costs for new plants [12]. These considerations have constituted the driving force

* Corresponding author. Fax: +41 44 633 1405.
E-mail address: jpr@chem.ethz.ch (J. Pérez-Ramírez).

0021-9517/$ - see front matter © 2011 Elsevier Inc. All rights reserved.
doi:10.1016/j.jcat.2011.11.016

to search for alternative cost-effective catalytic materials. A first step in this direction is the recent design of a copper delafossite ($CuAlO_2$) catalyst, which exhibited stable performance for more than 1200 h on stream [13]. However, this catalyst experienced significant copper loss.

CeO_2 (fluorite structure [14]) attracted our interest in view of its wide use in redox processes in many research fields [15–21] and oxidation reactions in particular [22–26]. In oxidations, it has been employed both as catalyst and co-catalyst. The success of CeO_2 stems from the easy generation of oxygen vacancies [22,27,28] that facilitate activation and transport of oxygen species. Nevertheless, only a few works have derived quantitative correlations between its oxidation activity and this structural peculiarity, typically measured in terms of oxygen storage capacity (OSC). Furthermore, comparisons have been preferably reported between CeO_2 and solid solutions of CeO_2 with ZrO_2 or SiO_2 [29], or between ceria-containing catalysts including supported (active) metal phases [30].

CeO_2-based materials have been claimed in the patent literature as catalysts potentially suited for HCl oxidation [31–33]. However, there are no studies gathering a fundamental understanding of the Deacon chemistry on CeO_2. Only the detailed assessment of CeO_2 activity and stability will determine its potential as an alternative to RuO_2-based catalysts for chlorine recycling.

Herein, we report on the use of CeO_2 in HCl oxidation, as well as on the fundamental knowledge derived by means of a multi-technique approach. Performance–structure–mechanism relationships are established, collecting information from extensive kinetic tests in a flow reactor at ambient pressure, detailed characterization (in relation to the catalyst activation procedure and the operating conditions), and mechanistic investigations using in situ infrared spectroscopy and density functional theory calculations.

2. Experimental

2.1. Catalysts

CeO_2 (Aldrich, nanopowder, code 544841) was calcined in static air at various temperatures in the range of 573–1373 K using a heating rate of 10 K min^{-1} and a dwell time of 5 h prior to use. These samples are referred to as "fresh." A complete list of all samples codes used along the manuscript, together with their description, is reported in Table 1.

2.2. Characterization

All the samples were subjected to basic characterization prior to and after catalytic testing. More extensive characterization was performed on CeO_2-773 and CeO_2-1173. In particular, fresh samples of these two catalysts were compared to samples exposed to reaction mixtures with feed O_2/HCl ratios equal to 2, 0.75, 0.25, or 0 (see Section 2.3 for detailed testing conditions).

Standard characterization of the samples was performed by powder X-ray diffraction (XRD), nitrogen adsorption at 77 K, and temperature-programmed reduction with hydrogen (H_2-TPR). The oxygen storage capacity (OSC) was measured by estimating the H_2 uptake of the samples (after a similar pre-treatment in inert gas as prior to the catalytic evaluation), as this represents an indirect quantification of the oxygen that the samples can store (Eq. (2)) [34–36].

$$CeO_2 + xH_2 \leftrightarrow CeO_{2-x} + xH_2O \quad (2)$$

This method was chosen among others reported in the literature [37], as the straightforward approach of determining the OSC by pulse chemisorption of oxygen [38] did not provide reproducible results on our samples. In order to select the appropriate temperature (573 K), at which the OSC would be evaluated in relation to a few outermost surface layers of CeO_2, the H_2 uptake was first separately measured at various temperatures (523–873 K), defined on the basis of the H_2-TPR profiles (Figs. S1–S2 in the ESI). The degree of bulk chlorination of selected catalysts after HCl oxidation was determined by thermogravimetric analysis coupled to mass spectrometry (TGA–MS). The structure, morphology, and composition of the catalyst particles were studied by high-resolution transmission electron microscopy (HRTEM). X-ray photoelectron spectroscopy (XPS) was applied to determine the degree of chlorination of the used CeO_2 catalysts. Three different layer models were employed to calculate the number of layers in CeO_2 that experienced chlorination. The first model was based on the inelastic mean free path (IMFP) and on 100% Cl occupation, the second on 80% of IMFP for practical effective attenuation length (EAL) and on 100% Cl occupation, and the third on 80% of IMFP for practical EAL and on 75% Cl occupation. For details on the characterization techniques, the reader is referred to the Electronic supplementary information (ESI).

Table 1
Description of catalysts' codes.

Catalyst code	Calcination temperature (K)	Catalyst state	Feed O_2/HCl ratio (mol mol^{-1})
CeO_2-573-F	573	Fresh	–
CeO_2-773-F	773	Fresh	–
CeO_2-1023-F	1023	Fresh	–
CeO_2-1173-F	1173	Fresh	–
CeO_2-1273-F	1273	Fresh	–
CeO_2-1373-F	1373	Fresh	–
CeO_2-573-2	573	Used	2
CeO_2-773-2	773	Used	2
CeO_2-1023-2	1023	Used	2
CeO_2-1173-2	1173	Used	2
CeO_2-1273-2	1273	Used	2
CeO_2-1373-2	1373	Used	2
CeO_2-773-0	773	Used	0
CeO_2-1173-0	1173	Used	0
CeO_2-1173-0.25	1173	Used	0.25
CeO_2-1173-0.75	1173	Used	0.75
CeO_2-1173-0.25-2	1173	Used	0.25 followed by 2
CeO_2-1173-0.25-7	1173	Used	0.25 followed by 7
CeO_2-1173-0-7	1173	Used	0 followed by 7

2.3. Catalytic tests

The oxidation of HCl with O_2 was carried out at ambient pressure in a quartz fixed-bed micro-reactor (8 mm i.d.) using 0.5 g of catalyst (particle size = 0.4–0.6 mm), a total flow of 166 cm^3 STP min^{-1}, a bed temperature (T_{bed}) of 703 K, and reaction times up to 3 h. The catalyst was kept at 703 K for 30 min in N_2 flow before admitting a mixture containing 10 vol.% HCl (Messer, purity 2.8, anhydrous) and 20 vol.% O_2 (Pan Gas, purity 5.0), balanced in N_2 (Pan Gas, purity 5.0).

Steady-state kinetic studies were performed on CeO_2-1173-F. First of all, it was experimentally verified that, under our experimental conditions, the reaction was not limited by extra- and/or intra-particle diffusion limitations. For this purpose, we varied (i) the total flow rate (83–250 cm^3 STP min^{-1}) at constant space time (W/F^0(HCl) = 11.2 g h mol^{-1}, defined as the ratio of the catalyst mass to the inlet molar flow of HCl) and (ii) the particle size (0.075–0.6 mm) with other conditions constant, respectively (Fig. S3 in the ESI). The kinetic experiments included changes of the feed composition at different temperatures and space times. In particular, the feed O_2/HCl ratio was varied in the range of 0.5–7 at constant feed HCl concentration (10 vol.%) and in the range 0.25–2 at constant feed O_2 concentration (10 vol.%) at T_{bed} = 603, 653, and 703 K and space times of 5.6, 9, and

11.2 g h mol^{-1}. CeO_2-1173-F samples exposed to O_2/HCl = 0, 0.25, or 0.75, and CeO_2-773-F treated in O_2/HCl = 0 (only HCl) at 703 K for 3 h were collected for characterization, after switching the feed to N_2 and allowing the reactor to cool down. In addition, experiments were carried out at 703 K combining a HCl-rich step, in which the catalyst was exposed to a feed composition O_2/HCl = 0 or 0.25 (causing bulk chlorination), and a O_2-rich step, in which substantial oxygen excess was supplied (O_2/HCl = 2 or 7). Cl_2 quantification at the reactor outlet was carried out by iodometric titration in a Metter Toledo G20 Compact Titrator, using the protocol reported elsewhere [39]. HCl conversion was determined from the Cl_2 produced, taking into account the reaction stoichiometry.

2.4. In situ Fourier transform infrared spectroscopy

A home-made transmission cell, especially designed to withstand the corrosive HCl oxidation mixture, was used for in situ Fourier transform infrared (FTIR) spectroscopy measurements. The sample in powder form was pressed into a self-supporting disc (15 mg cm^{-2}) under 30 bar for 10 s. The wafer, having a thickness of 50 μm, was placed in the sample holder, which also serves as the heating system. Inlet gases were analytical grade and controlled by mass flow controllers. The sample was heated in 20 vol.% O_2 in N_2 (100 cm^3 STP min^{-1}) up to 653 K (5 K min^{-1}) and allowed to stabilize. After ca. 1 h, 1 vol.% HCl was introduced into the O_2/N_2 flow to mimic a diluted Deacon feed condition. Spectra were recorded with a Varian-670 FTIR spectrometer at 653 K and with 4 cm^{-1} resolution.

2.5. Computational details

Density functional theory (DFT) simulations were applied to CeO_2 slabs. The calculations were performed with the 5.2 version of the VASP code [40]. The functional of choice was a GGA + U scheme to account in an approximate way for the complexity arising from the presence of *f*-electrons in cerium. The GGA was PBE [41], the U parameter chosen was set to 4.5 [42,43], and the inner electrons were replaced by PAW pseudopotentials [44]. The 12 valence electrons of Ce atoms in the 5*s*, 5*p*, 6*s*, 4*f*, and 5*d* states and the 6 valence electrons of O atoms in the 2*s* and 2*p* states were considered explicitly. The valence electrons were expanded in plane waves with a cutoff energy of 400 eV. For the bulk, the *k*-point sampling was $9 \times 9 \times 9$ [45]. The cell parameter obtained was 5.486 Å, in good agreement with experimental results and previous calculations [42,43]. The (1 1 1) facet was selected as it is known to be the lowest energy surface [43]. The chosen slab corresponds to a $p(2 \times 2)$ reconstruction and contains three layers. The *k*-point sampling was set to $3 \times 3 \times 1$ in this case. The calculated surface energy for this structure was 0.013 eV Å^{-2}. For this surface, several vacancy structures were considered and benchmarked against more accurate calculations in the literature employing hybrid methods [43]. When forming a vacancy or adsorbing on this surface, the systems were allowed to relax in all directions, except for the last layer of the slab. In all cases, the slabs were interleaved by 10 Å and decoupled from electronic interactions due to spurious polarizations given the asymmetry of the adsorption configuration. Spin-polarized calculations were performed when required. The CI-NEB method [46] was employed to locate the transition states, and the vibrational analysis of the potential transition state structures was performed to fully characterize the saddle points. In the calculation of vibrational frequencies, only the adsorbed structures of intermediates or transition states were considered. The numerical Hessian was calculated with two steps of 0.02 Å for each degree of freedom and then diagonalized to obtain the corresponding eigenvalues and eigenmodes.

3. Results and discussion

3.1. Catalytic evaluation

3.1.1. Influence of calcination temperature on activity

CeO_2 samples calcined at different temperatures were tested in the gas-phase catalytic oxidation of HCl in a continuous-flow fixed-bed reactor operated at ambient pressure and under isothermal conditions. XRD analysis showed that the fresh samples exhibited the characteristic reflections of cerium(IV) oxide. The HCl conversion over the samples ranged from 2% to 29% (Table 2), remaining essentially constant in the course of the 3-h test. Interestingly, the CeO_2 samples calcined at temperatures between 573 and 1173 K were similarly active, achieving the highest conversion levels, while higher calcination temperatures led to a progressive and almost complete depletion of the activity. These findings have been related to changes in the textural and structural properties of the materials and are first discussed on the basis of N_2 adsorption results. For the fresh catalysts, higher calcination temperatures led to lower total surface area (S_{BET}) values (Table 2). This result is expected, as higher temperatures favor sintering of the particles. The dependence of the HCl conversion on the S_{BET} of the fresh samples is shown in Fig. 1a (open symbols). For S_{BET} values > 25 m^2 g^{-1} (i.e., calcination temperature below 1173 K), the activity is independent of the S_{BET}, while for S_{BET} values < 25 m^2 g^{-1} (i.e., calcination temperature above 1173 K), it strongly depends on the surface area. In particular, CeO_2-1273-F (S_{BET} = 12 m^2 g^{-1}) and CeO_2-1373-F (S_{BET} = 1 m^2 g^{-1}), respectively, exhibited 14% and 2% HCl conversion, i.e., 2 and ca. 15 times lower activity than the other catalysts. Exposure of the catalysts to reaction conditions generally led to a drop in S_{BET} (Table 2). The change is significant for CeO_2-573-2, CeO_2-773-2, and CeO_2-1023-2, and evidences that substantial sintering of the CeO_2 particles occurred during HCl oxidation. In contrast, the S_{BET} values of CeO_2-1173-2, CeO_2-1273-2, and CeO_2-1373-2 were hardly affected, indicating that calcination at or above 1173 K resulted in stabilized materials in HCl oxidation. Calcination of the starting CeO_2 nanopowder at 1173 K provides the best compromise between performance and stability against sintering. Generally, the slope–plateau relation used to depict the dependence of activity on the S_{BET} of fresh samples turned out to be a good description for the used catalysts too (Fig. 1a, solid symbols). An experiment showing practically constant HCl conversion over CeO_2-773-F in contrast to a strongly decreasing S_{BET} with time-on-stream further supports the observed independence of the activity on S_{BET} for values of the latter greater than 25 m^2 g^{-1} (Fig. S4 in the ESI). It was accordingly concluded that another descriptor is needed to rationalize the HCl oxidation activity of CeO_2.

As mentioned in the introduction, the successful application of CeO_2-based materials in (electro) catalysis has been related to its capability to generate oxygen vacancies in the lattice [19,27]. Therefore, our CeO_2 samples were further investigated to assess

Table 2
Characterization and catalytic activity data.

Catalyst	S_{BET} [a] (m^2 g^{-1})		X_{HCl} [b] (%)	OSC [c] (μg O g$_{cat}^{-1}$)
	Fresh	Used		
CeO_2-573	117	46	29	–
CeO_2-773	106	27	25	390
CeO_2-1023	53	39	25	382
CeO_2-1173	30	25	27	376
CeO_2-1273	12	11	14	237
CeO_2-1373	1	1	2.1	78

[a] Total surface area, BET method.
[b] HCl conversion at O_2/HCl = 2, T_{bed} = 703 K, P = 1 bar, W/F^0(HCl) = 11.2 g h mol^{-1}.
[c] Oxygen storage capacity measured at 573 K.

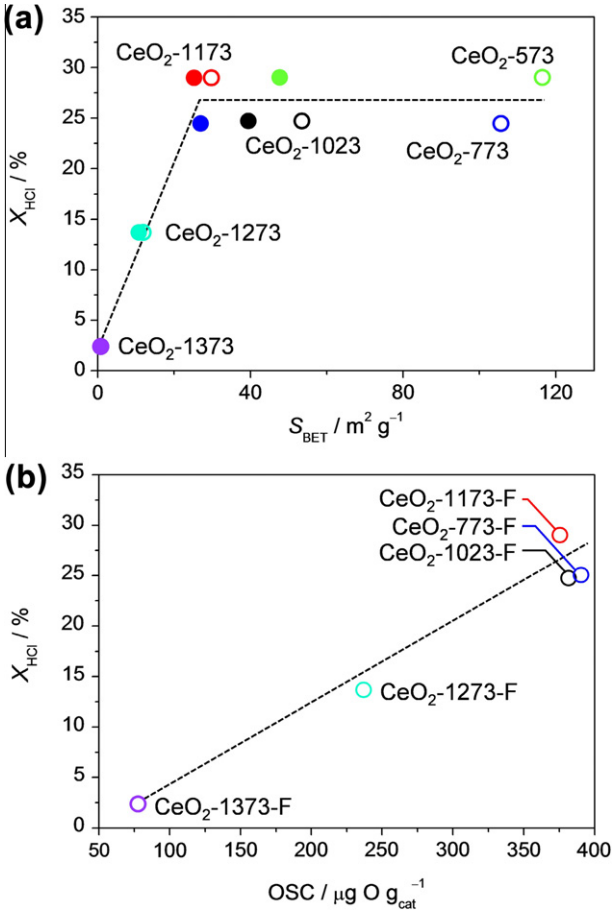

Fig. 1. HCl conversion *versus* (a) surface area of fresh (open symbols) and used (solid symbols) CeO_2 samples and (b) OSC, measured at 573 K, of fresh CeO_2 samples. Conditions: inlet mixture of 10 vol.% HCl and 20 vol.% O_2 balanced in N_2, T_{bed} = 703 K, W/F^0(HCl) = 11.2 g h mol^{-1}, P = 1 bar, and time-on-stream = 3 h.

their OSC, according to a method reported elsewhere [34]. On the basis of the values obtained (Table 2), the dependence of HCl conversion on OSC followed a linear trend (Fig. 1b). For CeO_2-773-F, CeO_2-1023-F, and CeO_2-1173-F, i.e., samples showing the highest (and similar) activity, the OSC was estimated at ca. 390 μg O g_{cat}^{-1}. For CeO_2-1273-F and CeO_2-1373-F, which exhibit decreasing HCl conversion levels, diminishing OSC values were measured, respectively, equal to 237 and 78 μg O g_{cat}^{-1}. Based on these results, the OSC proved to be a suitable parameter to rationalize the activity differences. Nevertheless, an influence of S_{BET} on OSC and/or a combined role of OSC and S_{BET}, when the latter is below 20 m^2 g^{-1}, on the catalytic activity could be considered. In this regard, Terribile et al. [47] showed that OSC, as measured for the bulk, was independent of S_{BET}. The outcome of this study might not be directly applicable to our case, in which OSC has to be considered limitedly to the outermost surface and subsurface layers of CeO_2, where the catalytic process takes place (vide infra). More generally, the OSC could be described as OSC = $S_{BET} \times \rho$, where ρ corresponds to the density of surface or near-surface oxygen vacancies. At higher temperatures, the Gibbs energy for vacancy formation decreases (see DFT results), thus favoring an increased generation of vacancies in the corresponding equilibrium conditions, but S_{BET} drops. This explains why a larger OSC, i.e., more active CeO_2, is found for samples calcined at 573–1173 K.

The activity of CeO_2 is significantly lower than that of RuO_2. A 40 K higher light-off temperature for Cl_2 evolution was determined over CeO_2-1173 by temperature-programmed reaction according to the protocol described in [39]. In view of a practical use, high-temperature operation is detrimental due to thermodynamic constraints that limit the equilibrium HCl conversion [48]. Nevertheless, these restrictions can be overcome by employing higher pressures and inlet O_2/HCl ratios, so that the degree of HCl conversion achieved still makes the development of a technical process feasible. Profiles of equilibrium HCl conversion at different total pressures and O_2/HCl ratios have been included in the ESI (Fig. S5a). Our experiments and calculations (vide infra) conclude that oxygen vacancies determine the activity of CeO_2 in HCl oxidation. More active ceria-based catalysts may be obtained enhancing its oxygen storage capacity, e.g., by the addition of dopants. However, this aspect was beyond the scope of the present manuscript.

3.1.2. Kinetic analysis

The influence of the O_2/HCl ratio on the activity was examined over CeO_2-1173-F at 703 K (Fig. 2). The HCl conversion increased upon raising the relative O_2 content in the feed mixture. The reaction order on O_2, calculated using a power equation fitting, was 0.5. This result suggests that oxygen-assisted chlorine evolution (re-oxidation) is the rate-limiting step, hence favored at a higher partial O_2 pressure. This point is further discussed in Section 3.4.3. Remarkably, the HCl conversion profiles derived from measurements in which the feed O_2 content was step-wise changed so to vary the O_2/HCl ratio from the lowest (0.5–7, Fig. 2 black symbols) or from the highest (7–0.5, Fig. 2, grey symbols) value evidence very little hysteresis (Fig. 2). This outcome indicates that the catalyst reversibly responds to variations of the feed mixture and highlights the dynamic character of the CeO_2 surface. The HCl conversion increased upon raising the space time for different feed O_2/HCl ratios (Fig. S6 in the ESI). On the contrary, the Cl_2 production decreased upon increasing the relative feed HCl content (Fig. S7 in the ESI), thus suggesting a change in the catalyst composition at the (near-)surface level (later addressed by characterization) that leads to activity loss. With regard to the dependency of CeO_2 activity on the reaction temperature, the HCl conversion level varied from 1% to 18% between 603 and 703 K at O_2/HCl = 2. The apparent activation energy was estimated at ca. 90 kJ mol^{-1}. In addition, a catalytic test using a feed mixture with O_2/HCl = 5 and an increased space time (at the limit of our current setup) was conducted. Fig. S5b in the ESI shows that a significant single-pass HCl conversion of 40% was reached over CeO_2 at 673 K and 1 bar.

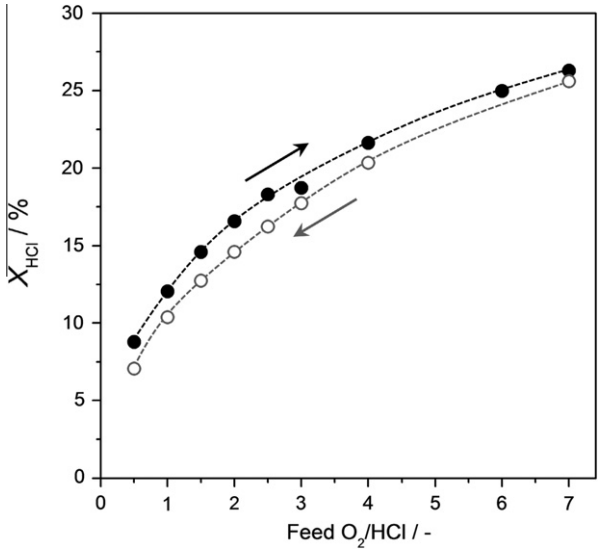

Fig. 2. HCl conversion *versus* feed O_2/HCl ratio at 703 K for CeO_2-1173-F. Conditions: inlet mixture of 10 vol.% HCl and 5–70 vol.% O_2 balanced in N_2, T_{bed} = 703 K, W/F^0(HCl) = 11.2 g h mol^{-1}, and P = 1 bar.

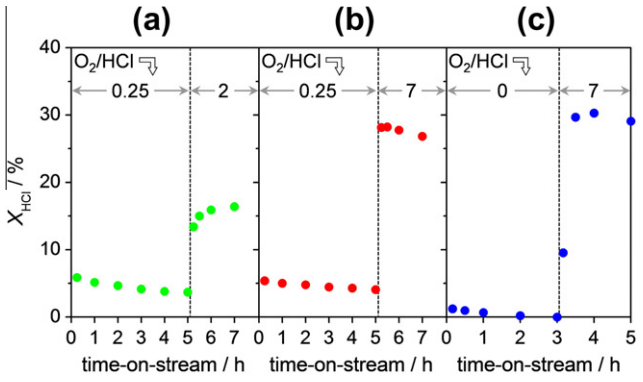

Fig. 3. HCl conversion *versus* time-on-stream over CeO_2-1173 using sequential HCl-rich/O_2-rich feed mixtures. (a) HCl-rich step with O_2/HCl = 0.25 followed by O_2-rich step with O_2/HCl = 2. (b) HCl-rich step with O_2/HCl = 0.25 followed by O_2-rich step with O_2/HCl = 7. (c) HCl-rich step with O_2/HCl = 0 followed by O_2-rich step with O_2/HCl = 7. Other conditions: T_{bed} = 703 K, W/F^0(HCl) = 11.2 g h mol^{-1}, and P = 1 bar.

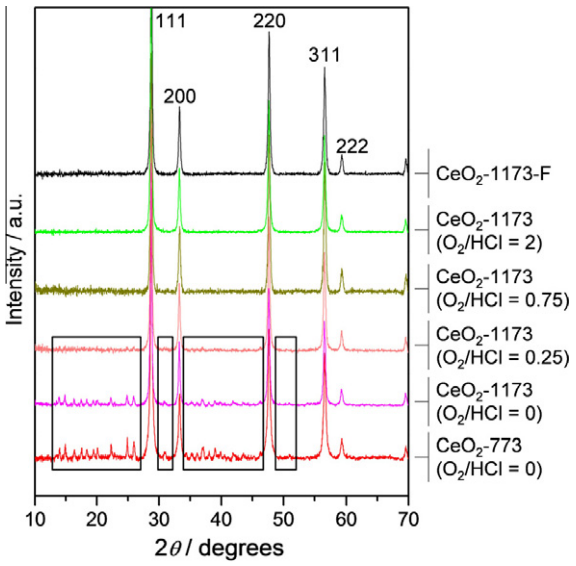

Fig. 4. XRD patterns of CeO_2-1173 samples in fresh and used (at various O_2/HCl ratios) forms. The diffractogram of CeO_2-773-0 is included for comparison. The most intense reflections are due to CeO_2 (JCPDS 73-6328), while those within boxes belong to $CeCl_3{\cdot}6H_2O$ (JCPDS 01-0149).

As operation in industry would be more economic lowering the inlet partial pressure of O_2 down to the stoichiometric amount (O_2/HCl = 0.25), we have investigated to which extent a stoichiometric or excess amount of HCl can negatively impact the catalytic activity. Some effort was also made to explore whether activity recovery is possible and to determine the re-oxidation kinetics. Fig. 3 displays the HCl conversion profiles obtained for CeO_2-1173-F in sequential HCl-rich/O_2-rich experiments. The HCl-rich step was conducted at 703 K using O_2/HCl = 0 or 0.25 for 3 or 5 h, followed by the O_2-rich step using O_2/HCl = 2 or 7 for 2 h. As shown in Fig. 3a, a slight decrease in HCl conversion was observed when the reaction was carried out with O_2/HCl = 0.25. Upon increasing the O_2 content in the feed (O_2/HCl = 2), a gradual increase in activity was obtained. The HCl conversion expected for an O_2/HCl = 2 feed composition (ca. 17%, Fig. 2) was approached in 2 h (Fig. 3a). In view of the slow re-oxidation kinetics, the experiment was repeated at a higher O_2/HCl ratio for the O_2-rich step. Using O_2/HCl = 7, the HCl conversion level immediately rose (Fig. 3b) to the expected value (ca. 27%, Fig. 2). When repeating this two-step experiment with the HCl-rich phase at O_2/HCl = 0 and the O_2-rich at O_2/HCl = 7, a similar profile was obtained (Fig. 3c). The data show that upon treating the catalyst with HCl in the absence of gas-phase O_2, the HCl conversion was completely depleted due to excessive chlorination (vide infra). Nevertheless, upon switching to O_2/HCl = 7, the original activity was fully restored within 1 h.

3.2. Characterization

3.2.1. X-ray diffraction and thermogravimetry

In order to relate the activity loss in HCl-rich feeds to modifications of the catalyst structure and/or composition, CeO_2-1173-F samples treated at 703 K for 3 h using various O_2/HCl feed ratios were analyzed by XRD (Fig. 4). The diffractogram of CeO_2-773-HCl is also included for comparison purposes. For the samples exposed to O_2/HCl = 0 or 0.25, $CeCl_3{\cdot}6H_2O$ (JCPDS 01-0149) reflections were detected, thus pointing to bulk chlorination as the main cause for the observed catalyst deactivation. From the intensity of the cerium chloride reflections, the samples could be sequenced according to the extent of bulk chlorination as follows: CeO_2-773-0 > CeO_2-1173-0 > CeO_2-1173-0.25. The fact that CeO_2-1173-0 was less altered than CeO_2-773-0 is probably related to the better stabilization achieved by high-temperature calcination, thus not only rendering lower sintering upon use, but also a higher resistance against chlorination. The presence of stoichiometric amounts of O_2 did not fully prevent structural alterations, but the degree of chlorination was smaller than for O_2-free runs. Samples treated in O_2/HCl = 0.75 or 2 did not suffer from detectable bulk chlorination. Accordingly, the choice of O_2/HCl feed ratio is of great importance and should be equal or higher than 0.75 to avoid activity deterioration of CeO_2-based catalysts. The inhibiting effect of excess HCl on the conversion (Fig. S7 in the ESI) can be related to bulk chlorination. Deactivation does not appear to be induced by the volatilization of the active phase in form of the metal chlorides produced in situ, as in the case of copper-based catalysts [13,39]. Analysis of the condensate at the reactor outlet by ICP-OES did not show appreciable cerium loss. On the basis of the result of the catalytic test on $CeCl_3$ (HCl conversion = 2%, at 703 K and O_2/HCl = 2), the activity loss is assigned to the inactivity of cerium chloride for HCl oxidation.

XRD analysis of the samples exposed to the HCl-rich/O_2-rich mixtures (Fig. S8 in the ESI) evidenced that activity recovery was indeed induced by the removal of chlorine at higher partial pressures of O_2. In the case of the samples treated with O_2/HCl = 7, the original CeO_2 phase was restored, while traces of $CeCl_3{\cdot}6H_2O$ were still observed for the sample exposed to a lower oxygen excess (O_2/HCl = 2). These evidences are in line with the activity pattern described above.

Quantification of the chlorination degree was estimated by TGA-MS studies of the used catalysts. The weight loss and MS profiles as a function of the temperature are reported in Fig. S9 in the ESI. According to these data, the values for molar Cl/Ce ratio were 0.38, 0.30, and 0.08 for CeO_2-773-0, CeO_2-1173-0, and CeO_2-1173-0.25, respectively. These results support the trend qualitatively derived by XRD.

In contrast to the extensive bulk alteration reported for CuO and MnO_2 already upon exposure to an O_2-rich feed (O_2/HCl = 2) [39,49], chlorination of CeO_2 occurs only under stoichiometric feed conditions or in excess HCl and to a very limited extent. Consequently, the behavior of CeO_2 resembles more that of RuO_2, and this is directly related to the high stability of the latter two oxides in the Deacon reaction.

3.2.2. High-resolution transmission electron microscopy

TEM micrographs of CeO_2-773-F reveal a bimodal particle size distribution (Fig. 5a). Small CeO_2 particles of approximately

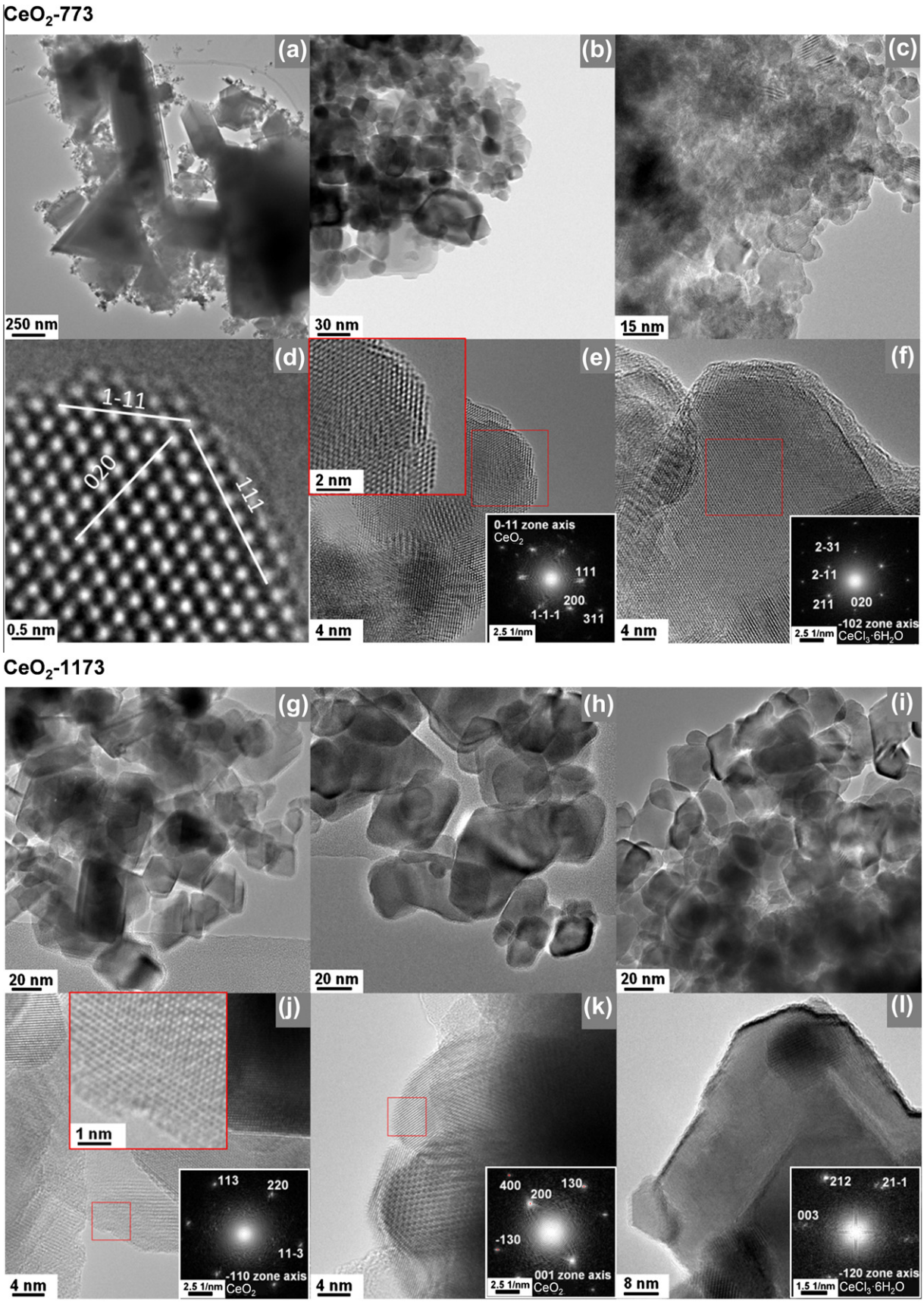

Fig. 5. TEM of (a) CeO_2-773-F, (b) CeO_2-773-2, (c) CeO_2-773-0, and HRTEM of (d) CeO_2-773-2, revealing the surface of the CeO_2 particles. (e) A CeO_2-773-0 particle (surface termination in the inset) and (f) a CeO_2-773-0 particle showing an amorphous surface layer of $CeCl_3{\cdot}6H_2O$. TEM of (g) CeO_2-1173-F, (h) CeO_2-1173-2, and (i) CeO_2-1173-0. Detailed imaging of (j) CeO_2-1173-2, showing CeO_2 particles with clean surface (inset) and of (k and l) CeO_2-1173-0, exhibiting both the (k) CeO_2 and (l) $CeCl_3{\cdot}6H_2O$ phases.

10 nm are scattered around larger particles reaching up to 300 nm. Exposure to O_2/HCl = 2 induced a significant change in particle size (CeO_2-773-2), which attained a range of 20–40 nm (Fig. 5b). Under Deacon conditions, the smaller particles agglomerated and the bigger particles "cracked", thus not being detectable in the used sample. While sintering is expected to occur upon use, the latter phenomenon is tentatively explained on the basis of a different activity/stability of the crystal facets, where one (or more) might be unstable under reaction conditions. It cannot be excluded that the mechanical strain applied in the pressing step during preparation of the sieve fraction may be the origin of the disruption of the bigger grains. Nevertheless, the significantly reduced S_{BET} of CeO_2-773-2 implies that the loss in surface area determined by the agglomeration of the small particles clearly surpasses the increase due to the disruption of few big grains. High-resolution imaging of the surface of CeO_2 nanoparticles after exposure to Deacon conditions shows clean surfaces exhibiting several steps (Fig. 5d). The analysis of CeO_2-773-0 reveals some clear changes due to the treatment in HCl only. While the size of the nanoparticles does not seem to differ significantly from CeO_2-773-2 (Fig. 5c), the treatment had a considerable effect on the particle structure. Besides rounded nanoparticles of CeO_2-773-0 (Fig. 5e), revealing numerous "clean" atomic steps on the surface (magnified in the inset of Fig. 5e), nanoparticles covered with an amorphous layer are now evidenced (Fig. 5f). SAED (selected area electron diffraction) analysis of such particles suggests that the structure can fit to $CeCl_3{\cdot}6H_2O$, in agreement with the phase assigned by XRD (Fig. 4). The high vacuum conditions of the TEM could result in the removal of crystal water from the $CeCl_3{\cdot}6H_2O$ particles, leading to a collapse of the structural order in the near-surface region. This would explain the amorphous layer covering the particles. The coexistence of clean CeO_2 particles and particles made of $CeCl_3{\cdot}6H_2O$ substantiates that certain crystallographic planes of CeO_2 are less prone to chlorination while others favor the formation of the chloride phase.

The catalyst morphology within the complete "1173"-series (Fig. 5g–i) looks substantially similar, with the particle size ranging between 20 and 40 nm in all the samples. The fresh catalyst does not contain considerable amounts of bigger particles as in CeO_2-773-F. Thus, the particle size was stabilized already during calcination at the higher temperature, an effect that apparently occurred for the CeO_2-773-F sample only after exposure to Deacon conditions. The only assigned phase in CeO_2-1173-2 was CeO_2 (Fig. 5j). In CeO_2-1173-0, both CeO_2 (Fig. 5k) and $CeCl_3{\cdot}6H_2O$ (Fig. 5l) were present. SAED analyses showed that CeO_2 is the dominant structure in the CeO_2-1173-0 sample with a minor $CeCl_3{\cdot}6H_2O$ contribution. This result also agrees with XRD (Fig. 4).

3.2.3. X-ray photoelectron spectroscopy

XPS was applied to selected catalysts to assess the degree of surface chlorination. Table 3 compiles the experimentally determined Cl/Ce ratios. In general, CeO_2-773-F was more prone to chlorination than CeO_2-1173-F. Moreover, exposure to HCl gave rise to a more extended chlorination than the exposure to HCl + O_2. Both findings are in line with XRD analyses. To translate the Cl/Ce stoichiometry numbers that assume homogeneous distribution of Cl in the information depth into the number of near-surface layers containing Cl, various models were applied (see details in the ESI). Thus, a more realistic layered structure was constructed (Cl occupation preference from top inwards) giving rise to the same signal ratio as determined by XPS. As Table 3 indicates, Cl occupies approximately 1–1.5 layers in the samples used under Deacon conditions and 2.5 to 6 layers after HCl conditioning. Nevertheless, one should remember that after exposure to the mixture, the samples were quenched in N_2; thus, it is reasonable to assume that the Cl atoms adsorbed on external Ce atoms could desorb and hence are not counted in XPS. This assumption is in line with DFT simulations (Section 3.4.3). Based on the XPS data, it can be concluded that during HCL oxidation, Cl atoms can occupy surface sites as well as lattice oxygen vacancies. This is in contrast to the RuO_2 case, where chlorination was confined to the surface layer [9,10,51]. Since XRD after HCl treatment detected traces of $CeCl_3{\cdot}6H_2O$, the higher Cl uptake in the near-surface region for CeO_2-1173-0 and CeO_2-773-0 can be explained by the presence of the chloride phase. The Ce 3*d* difference spectrum (Fig. S10 in the ESI) between 773-0 and 773-F confirms the presence of $CeCl_3{\cdot}6H_2O$. The calculation, indicating 8% of chloride phase (corresponding to an increase in Cl/Ce by ca. 0.24), is in reasonable agreement with the observed increase in Cl/Ce by 0.36, and the difference might be due to additional subsurface Cl occupation. In addition, Fig. S10 in the ESI suggests that calcination at 773 K is not sufficient to produce fully oxidized cerium (CeO_2), an extra 10% of Ce^{3+} state being estimated after this milder calcination.

Table 3
Quantification of the surface Cl uptake from XPS measurements, using different models.

Catalyst	Cl/Ce stoichiometry[a]	Number of layers occupied by Cl		
		Model 1 IMFP[b]	Model 2 EAL[c]	Model 3 EAL, 75% Cl[d]
CeO_2-773-F	–	–	–	–
CeO_2-773-2	0.19	1.5	1.2	1.6
CeO_2-773-0	0.55	5.7	4.6	6.1
CeO_2-1173-F	–	–	–	–
CeO_2-1173-2	0.14	1.0	0.8	1.1
CeO_2-1373-0	0.29	2.4	1.9	2.6

[a] Based on homogeneous distribution of elements.
[b] Inelastic mean free path (by TPP-2 M [50]): 22 Å.
[c] Effective attenuation length, 0.8×IMFP was used.
[d] Additionally, to the EAL model, 75% Cl occupation of possible sites was considered, in line with the DFT calculations.

3.3. In situ Fourier transform infrared spectroscopy

In situ FTIR experiments were carried out to study the chlorination mechanism indirectly, that is, following the evolution of the OH stretching bands upon introducing a diluted Deacon feed. A detailed description based on our DFT analysis of different configurations of OH/H_2O-related species adsorbed on CeO_2(1 1 1) and of the corresponding vibrational frequencies is presented in the ESI (Table S1). The CeO_2-773-F sample was activated by heating in O_2/N_2 up to 653 K and holding at this temperature till no spectral changes were observed. The spectrum at the end of this stage (Fig. 6, dark blue) shows two main bands at 3713 and 3632 cm^{-1}, which are, respectively, assigned to mono-coordinated (OH-I) and bridging (OH-IIB) hydroxyls [52–54]. Another absorption band at 3684 cm^{-1}, due to water, as well as a band at 3660 cm^{-1}, attributed to a different bridging hydroxyl species (OH-IIA), vanished during the activation process. The existence of two types of bridged hydroxyl groups was first reported by Badri et al. [52], who assigned the red-shifted band to bridged hydroxyl groups next to oxygen vacancies created by water elimination. According to our DFT calculations on CeO_2(1 1 1), the mono-coordinate OH band should appear at 3729 cm^{-1}, but threefold coordinated OH species with surface O being part of the lattice can also give rise to bands in the range of 3750–3732 cm^{-1}. Note that the calculation tends to overestimate the stretching frequency by 15–30 cm^{-1} when benchmarked against gas-phase water molecules. Additionally, OH-II species seem to be unstable on the (1 1 1) and (1 0 0) facets. On the other hand, bands related to water with a neighboring hydroxyl group are expected to fall around

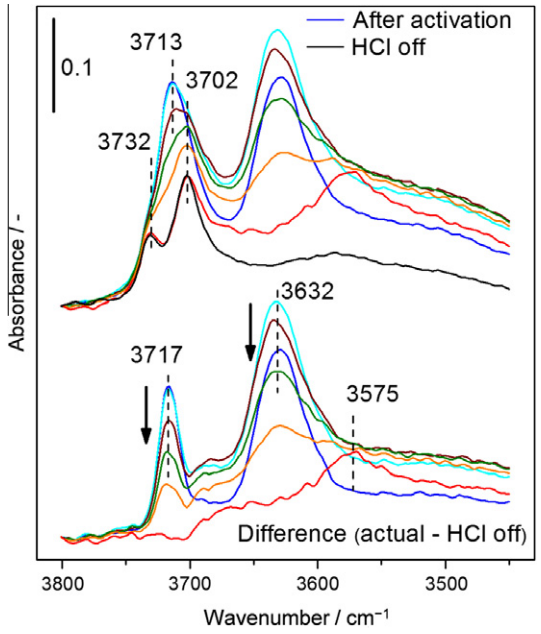

Fig. 6. Evolution of the stretching OH band region of CeO_2-773-F upon introducing 1 vol.% HCl into an O_2/N_2 (20/80) feed at 653 K. The dark blue curve represents the starting state prior to HCl introduction, whereas the black spectrum shows the stabilized state after HCl has been turned off (both in O_2/N_2). The temporal evolution in the Deacon feed was as follows: light blue/brown/green/orange/red corresponding to time-on-stream of 85/170/220/270/1055 s, respectively. (For interpretation of the references to color in this figure legend, the reader is referred to the web version of this article.)

3682–3646 cm^{-1}; thus, they may give rise to the low-frequency absorption.

Two shoulders at 3732 cm^{-1} and 3702 cm^{-1} are visible on both sides of the high-frequency OH band. Upon introducing HCl in the O_2/N_2 feed, these shoulders became more resolved. According to Table S1, they can be attributed to threefold coordinated hydroxyl groups, as well as to mono-coordinated OH groups with different neighboring species coexisting on the surface. During HCl oxidation, significant changes were observed in the spectra, as the intensity of the peak at 3632 cm^{-1} decreased gradually till it was completely depleted at later stages (Fig. 6, light blue till red). According to the bands assignment in the OH stretching region suggested by our DFT-calculated vibrational frequencies, this would indicate that the initial H_2O–OH pairs progressively disappeared, likely due to the partial occupation of the vacancies by Cl. OH–Cl pairs showed OH vibration at 3739 cm^{-1}, just in the middle of the OH band of threefold and adsorbed OH. In parallel, the baseline in the whole spectral region first increased (light blue/brown/green), and, then declined to reach the level shown by the red spectrum. This modulation of the baseline reflects the rapid evolution, desorption, and stabilization of the hydrogen-bonded water structure as HCl dissociatively adsorbs on the ceria surface. The broad signal at 3575 cm^{-1} (red spectrum), developed when the hydrogen-bonded water structure reached low enough concentration, can be assigned to isolated adsorbed water species produced during the reaction (in line with the theoretical value at 3591 cm^{-1}), since it diminished after stopping the HCl flow (black line). To visualize the changes occurring in the high-frequency OH band, the "HCl off" curve was subtracted from all other spectra. This illustration suggests that the changes in this band were not due to band shift, but rather related to the gradual disappearance of one OH species at 3717 cm^{-1} in parallel with the depletion of the band at 3632 cm^{-1}. This experiment suggests that surface chlorination occurs *via* dissociative HCl adsorption (baseline modulation) and consumption of OH groups, and thus through the displacement of surface oxygen species of different coordination by Cl.

3.4. Molecular modeling

3.4.1. Vacancy formation, diffusion, and healing

The surface energy to cleave the (1 1 1) plane of CeO_2(1 1 1) is 0.013 eV $Å^{-2}$. The inward relaxation of the external atoms is 0.090 and 0.097 Å for Ce and O atoms, respectively. The material is known to be easily reducible and, thus, can accommodate oxygen vacancies [55]. The formation of surface vacancies, thereafter denoted as □, in 0.25 ML (monolayers) in the $p(2 \times 2)$ cell is endothermic by 3.25 eV. This is a very small value when compared to ionic materials [56] or to other reducible oxides like $SrTiO_3$ [57]. The electronic structure of the surface vacancy corresponds to an anti-ferromagnetic solution, where the two electrons left end up in the next and next nearest surface Ce atoms, as described by Ganduglia-Pirovano et al. [43]. The electronic structure, electron localization, and formation energy are in good agreement with previous calculations with both PBE + U and HSE06 functionals [43]. The latter is supposed to be more accurate for strongly localized *f*-electrons. However, the energy difference with other configurations is rather small and dynamic re-ordering of the electronic structure through polaronic effects is likely to occur [58,59].

Oxygen vacancies can be present in near-surface layers (Fig. 7c). Indeed, the formation energy for subsurface defects turns out to be lower than for surface defects, 2.93 eV, in agreement with previous theoretical estimates [43]. The energy requirement for surface to subsurface vacancy diffusion is small, 0.30 eV, in line with reported values for bulk diffusion, 0.50 eV [60]. Vacancy agglomeration has also been evidenced by scanning tunneling microscopy (STM) investigations [28]. From our calculations on a $p(4 \times 2)$ supercell, surface vacancy agglomeration at a constant concentration of 0.25 ML is weakly exothermic, by 0.13 eV, in agreement with STM images [28].

As for the surface re-oxidation, oxygen adsorption does not take place on a non-defective CeO_2(1 1 1) surface, but occurs on surface oxygen vacancies, □, leading to a superoxo-like species, in which one of the two O atoms fills the hole, and the O–O distance is 1.453 Å. Dissociation of this bond heals the defect and leaves a surface O atom, but it is uphill by 1.80 eV. Nevertheless, the dynamics of oxygen vacancies in oxides can be enhanced by the presence of gas-phase O_2 [61]. Aggregation of oxygen defects at the surface or near-surface is energetically favored. Indeed, surface vacancy diffusion takes place by penetration to the subsurface layer and ejection toward the surface in neighboring lattice position. The first step is exothermic by 0.72 eV with a barrier of 0.24 eV, while the second is mildly endothermic (0.59 eV) with a barrier of 0.64 eV. Once the defect dimer is present on the surface, gas-phase oxygen molecules can interact healing both vacancies and liberating about 6 eV.

3.4.2. Chlorination

In order to assess the stability of CeO_2(1 1 1), we have employed first-principles thermodynamics [62] to consider the effect of partial oxygen and chlorine pressures on the state of the surface. The stability problem is considerable and was simplified by exclusively considering a reactant (O_2) and a product (Cl_2), for which no crossing between the associated chemical potentials appears in the equations. The excess surface energy can be calculated from the following equation:

$$\Delta G_X \approx E_X - E_{CeO2} + N_{O2}/2\mu_{O2} - N_{Cl2}/2\mu_{Cl2} \quad (3)$$

where ΔG_X is the Gibbs energy associated with the configuration *X* with respect to the energy of regularly terminated CeO_2 (E_{CeO_2}) N_{O_2} and N_{Cl_2} are the number of oxygen and chlorine molecules, and μ is the corresponding gas-phase chemical potential. The ability of HCl

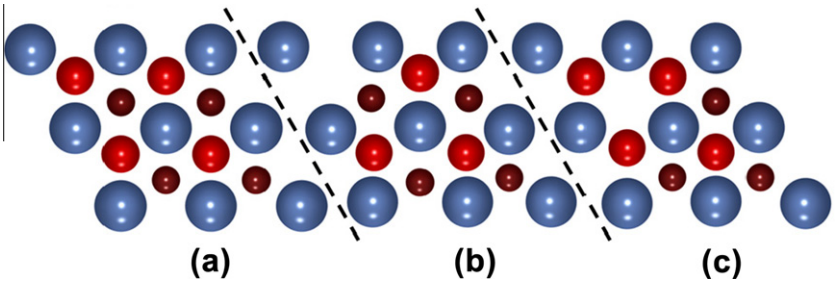

Fig. 7. Structural model of a $p(2 \times (2)$ supercell of $CeO_2(1\,1\,1)$: (a) regular surface, (b) surface vacancy, and (c) subsurface vacancy. Ce atoms are depicted in blue, surface O atoms in red, and subsurface O atoms in scarlet and small balls.

to form chlorides is somehow higher than that of Cl_2, but the present model serves as a guide to evaluate the degree of chlorination of the material. The Gibbs potentials of solids including 40 different X configurations, E_X, and of the regular surface, E_{CeO_2}, were taken from DFT calculations, and the chemical potentials of Cl_2 and O_2 were calculated through statistical thermodynamics [63]. Fig. S11 in the ESI shows that, at extremely low oxygen and chlorine chemical potentials, the surface is regularly terminated. When increasing the Cl_2 pressure, partial chlorination can take place by substitution of an oxygen atom from the surface (Fig. S11 in the ESI, green configuration). At relatively low oxygen pressures (for $\log(pO_2)$ and $\log(pCl_2)$ in the range -1 to 2), the clean surface, mono-substituted Cl, and multiple substituted Cl structures lie very close in energy and are likely present on the catalyst surface. If the chlorine pressure is much higher ($\log(pCl_2) = 0$), lattices with Cl in lattice oxygen positions become more stable. The maximum oxygen substitution achievable in this way corresponds to 50% of the surface oxygen atoms. If the oxygen pressure is raised up to the 0.1 bar regime, as in our catalytic tests, then the most likely configuration corresponds to the clean surface. Finally, the thermodynamic penalty to introduce a Cl atom occupying a vacancy site (Cl□) to inner layers is about 3 eV. Accordingly, it is implied that Cl preferentially stays in the near-surface region, and that high HCl or Cl_2 pressures might account for lattice disruption and formation of $CeCl_3$-related phases (Section 3.2), as Cl cannot be accommodated in the bulk of CeO_2.

3.4.3. Reaction mechanism

The reaction profile of the HCl oxidation on CeO_2 is presented in Fig. 8. The main elementary steps derived for the Deacon process comprise (i) hydrogen abstraction from HCl by basic surface O atoms, to form hydroxyl groups and leave chlorine atoms on the surface, (ii) reaction of the hydroxyl groups with new incoming HCl molecules and/or hydroxyl group recombination on the surface to form water, (iii) water removal, (iv) re-oxidation, and (v) recombination of chlorine atoms.

The Deacon reaction starts by the adsorption of HCl near the basic centers on the surface (lattice oxygen atoms, O_{lat}). The reaction is energetically favored provided that a surface vacancy exists, where the Cl atom can be accommodated (Fig. 8, step A). In this process, HCl adsorption is exothermic by 2.84 eV and leads to a surface $O_{lat}H$ group and a Cl atom at the surface vacancy. Care should be taken as both O_{lat} and adsorbed O atoms can give rise to the OH-I and OH-II vibrational bands described in Section 3.3. At the transition state, the Cl–H and O_{lat}–H distances are 3.590 and 2.121 Å, respectively. A second HCl molecule can adsorb, forming a water molecule and leaving a Cl atom on top of a Ce atom on the surface, Cl^* (Fig. 8, step B). This second process is also exothermic, but only by 0.29 eV. The external Cl^* atom can push the already formed water molecule H_2O_{lat} out of the lattice and fill the nascent vacancy, thus becoming Cl□. This process is almost thermo-neutral (Fig. 8, step C). Then, one of the oxygen atoms from the subsurface layer can diffuse toward the surface, pushing a

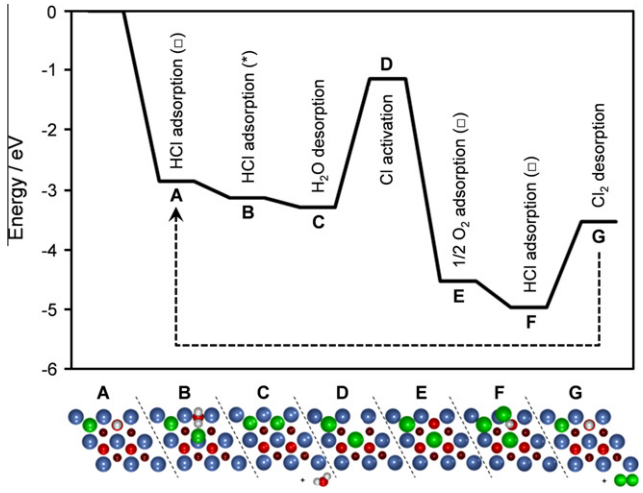

Fig. 8. Reaction energy profile for the Deacon process on $CeO_2(1\,1\,1)$. The initial state in the profile is $CeO_2(1\,1\,1)$ with a surface oxygen vacancy (Fig. 7b). The color codes in the bottom panels are as described in the caption of Fig. 7.

Cl□ atom toward the outer surface, i.e., converting Cl□ in Cl^* (Fig. 8, step D). The energy required for this elementary step is 2.15 eV and forms an oxygen vacancy at a subsurface position, $□_{ss}$. Re-oxidation can take place by the complex diffusion–reaction mechanism described in Section 3.4.1 to release nearly 3.4 eV (Fig. 8, step E). Still, HCl can adsorb on this surface releasing 0.42 eV to form a $O_{lat}H$ and a Cl^* (Fig. 8, step F). Three chlorine atoms are then adsorbed on the surface, one Cl^* and two Cl□, respectively. Cl_2 evolution toward the gas phase takes place from this structure; the energy required is 1.42 eV (Fig. 8, step G). As it can be noticed in Fig. 8, states A and G correspond to the active states of the catalyst. Therefore, the catalytic cycle runs between steps A and G.

The list of elementary steps in the mechanism can be summarized by the following reactions:

$$HCl + O_{lat} + □ \rightarrow O_{lat}H + Cl□ \quad (4)$$

$$HCl + O_{lat}H + * \rightarrow H_2O_{lat} + Cl^* \quad (5)$$

$$Cl^* + H_2O_{lat} \rightarrow Cl□ + H_2O \quad (6)$$

$$Cl□ + * \rightarrow □ + Cl^* \quad (7)$$

$$□ + 1/2O_2 \rightarrow O_{lat} \quad (8)$$

$$Cl^* + Cl^* \rightarrow Cl_2 + 2^* \quad (9)$$

It is important to notice that, although the reaction scheme on CeO_2 resembles that of RuO_2, some important differences are found. First, the reaction on RuO_2 occurs at almost full coverage of the under-

Table 4
Energy (ΔE) in eV and Gibbs free energy (ΔG^0) in kJ mol^{-1} M (M = Ce, Ru) atom for the complete chlorination of CeO_2 and RuO_2 by Cl_2 or HCl.[a]

Chlorination equation	ΔE	$\Delta G°$	
		573 K	703 K
$CeO_2 + 3/2Cl_2 \rightarrow CeCl_3 + O_2$	15.82	92.95	112.18
$CeO_2 + 4HCl \rightarrow CeCl_3 + 2H_2O + 1/2Cl_2$	−115.99	60.61	97.95
$RuO_2 + 3/2Cl_2 \rightarrow RuCl_3 + O_2$	101.86	178.98	198.22
$RuO_2 + 4HCl \rightarrow RuCl_3 + 2H_2O + 1/2Cl_2$	−29.95	146.65	183.98

[a] Calculated using the PBE (RuO_2) and PBE + U (CeO_2) functionals.

coordinated Ru_{cus} positions, as nearly all available sites are occupied by Cl [9]. For CeO_2, under-coordinated cerium atoms only exist when oxygen vacancies are present in the surface or near-surface regions. These are the only active sites for the reaction, in agreement with the linearity found between activity and OSC (Fig. 1b). As a consequence, the reaction profile for CeO_2 is much more abrupt (involves higher energy requirements) than that of RuO_2. This correlates with the higher temperatures needed to run the Deacon reaction on CeO_2 (vide supra). The most energy-demanding step of HCl oxidation on RuO_2 is related to the formation and evolution of Cl_2. Due to the high energy required for Cl_2 elimination on RuO_2, Cl self-poisoning is observed, and thus, re-oxidation turns out to be the rate-determining step under relevant conditions, as shown by the positive dependence of the activity on the partial pressure of O_2 [51]. For CeO_2, the activation of Cl atoms from lattice vacancies to surface positions is the most energy-demanding step.

The similar activity enhancement observed at higher partial O_2 pressures (Fig. 2) can be rationalized on the basis of the chlorine and oxygen competition for the same active sites, which tightly couples chlorine elimination to oxygen re-adsorption. When Cl atoms occupy most of the active positions, very few active sites exist for re-oxidation, thus producing less Cl_2. In extreme cases, this leads to catalyst deactivation.

Regarding the stability against the harsh reaction conditions employed, while the experimental data indicate that RuO_2 and CeO_2 are quite similar, the DFT analysis points out some differences. The RuO_2 surface is known to be partially chlorinated, but this chlorination is confined to the under-coordinated O and Ru positions at the external surface. Comparing surface Cl contents, the situation is such that the amount of Cl on the surface of RuO_2 is very large, as the under-coordinated positions in the lattice are very prone to adsorb reactants (Cl in particular). This effect is less evident on CeO_2, given the relative inertness of Ce atoms on the surface. Indeed, most of the Cl is sitting at oxygen vacancies on the surface and not directly on top of the active Ce sites. In addition, the penetration of Cl atoms to deeper layers is hindered in both RuO_2 and CeO_2 systems by more than 2 eV. This energy is somewhat larger for CeO_2 (3 eV). Nevertheless, owing to vacancy diffusion, and thus oxygen supply to the surface, ceria will be more prone to subsurface and bulk chlorination in pure HCl or sub-stoichiometric Deacon feeds. In line with this, we have compared the energy required for the bulk chlorination and lattice disruption in both Ru and Ce cases (Table 4). The energy requirement for the chlorination of CeO_2 is smaller than the corresponding value for RuO_2, in agreement with the greater chlorination detected in the CeO_2 experiments in HCl-rich feeds.

4. Conclusions

In this study, we present a fundamental understanding of HCl oxidation on bulk CeO_2 combining catalyst testing, steady-state kinetics, characterization, and DFT simulations. Due to its remarkable activity and stability, CeO_2 constitutes a promising alternative to highly expensive RuO_2-based catalysts for industrial chlorine recycling. The activity is related to the presence of oxygen vacancies in the material. The stability arises from the remarkable resistance of cerium oxide against chlorination. Limited bulk chlorination, that is detection of $CeCl_3$ by XRD, takes place under HCl-rich conditions ($O_2/HCl \leqslant 0.25$). The bulk chloride phase rapidly and completely disappears when the catalyst is exposed to O_2-rich conditions. Under $O_2/HCl \geqslant 0.75$, only the outermost surface layers of CeO_2 contain chlorine. Density functional theory simulations reveal that Cl activation from vacancy positions to surface Ce atoms is the most energy-demanding step, although chorine–oxygen competition for the available active sites may render re-oxidation as the rate-determining step. Current studies focus on developing a proper strategy to support the active phase on a suitable carrier preserving the catalytic proprerties of bulk CeO_2.

Acknowledgment

We thank Bayer MaterialScience for permission to publish these results.

Appendix A. Supplementary material

Electronic Supplementary Information (ESI): Experimental details of the applied characterization techniques, additional results from characterization, catalytic testing, and DFT simulations. The above material can be found, in the online version, at doi:10.1016/j.jcat.2011.11.016.

References

[1] J. Pérez-Ramírez, C. Mondelli, T. Schmidt, O.F.-K. Schlüter, A. Wolf, L. Mleczko, T. Dreier, Energy Environ. Sci. 4 (2011) 4786.
[2] K. Seki, Catal. Surv. Asia 14 (2010) 168.
[3] H. Deacon, US Patent 85,370, Assigned to Gaskell, Deacon and Co., 1868.
[4] A.J. Johnson, A.J. Cherniavsky, US Patent 2542,961, Assigned to Shell Development Company, 1951.
[5] T. Kiyoura, N. Fujimoto, M. Ajioka, T. Suzuki, Y. Kogure, K. Kanaya, T. Nagayama, EP184413-A, Assigned to Mitsui Toatsu Chemicals, 1984.
[6] T. Hibi, H. Nishida, H. Abekawa, US Patent 5871,707, Assigned to Sumitomo Chemical Company, 1999.
[7] C. Mondelli, A.P. Amrute, F. Krumeich, T. Schmidt, J. Pérez-Ramírez, ChemCatChem 3 (2011) 657.
[8] A. Wolf, L. Mleczko, O.F. Schlüter, S. Schubert, EP2026905, Assigned to Bayer MaterialScience, 2006.
[9] M.A.G. Hevia, A.P. Amrute, T. Schmidt, J. Pérez-Ramírez, J. Catal. 276 (2010) 141.
[10] D. Crihan, M. Knapp, S. Zweidinger, E. Lundgren, C.J. Weststrate, J.N. Andersen, A.P. Seitsonen, H. Over, Angew. Chem. Int. Ed. 47 (2008) 2131.
[11] J.P. Hofmann, S. Zweidinger, A.P. Seitsonen, A. Farkas, M. Knapp, O. Balmes, E. Lundgren, J.N. Andersen, H. Over, Phys. Chem. Chem. Phys. 12 (2010) 15358.
[12] Retrieved from <http://www.platinum.matthey.com/pgm-prices>.
[13] C. Mondelli, A.P. Amrute, T. Schmidt, J. Pérez-Ramírez, Chem. Commun. 47 (2011) 7173.
[14] R.W.G. Wyckoff, Crystal Structures, Interscience, New York, 1965.
[15] R.J. Gorte, AIChE J. 56 (2010) 1126.
[16] Q. Fu, H. Saltsburg, M. Flytzani-Stephanopoulos, Science 301 (2003) 935.
[17] A. Primo, T. Marino, A. Corma, R. Molinari, H. Garcia, J. Am. Chem. Soc. 133 (2011) 6930.
[18] Y.S. Chaudhary, S. Panigrahi, S. Nayak, B. Sarpati, S. Bhattacharjee, N. Kulkarni, J. Mater. Chem. 20 (2010) 2381.
[19] M. Mogensen, N.M. Sammes, G.A. Tompsett, Solid State Ion. 129 (2000) 63.
[20] B. Zhu, M.D. Mat, Int. J. Electrochem. Sci. 1 (2006) 383.
[21] F. Zhou, X. Zhao, H. Xu, C. Yuan, J. Phys. Chem. C 111 (2007) 1651.
[22] A. Trovarelli, Catal. Rev.–Sci. Eng. 38 (1996) 439.
[23] A. Gómez-Cortés, Y. Márquez, J. Arenas-Alatorre, G. Díaz, Catal. Today 133–135 (2008) 743.
[24] A. Martínez-Arias, A.B. Hungría, G. Munuera, D. Gamarra, Appl. Catal. B 65 (2006) 207.
[25] W. Shin, C. Jung, J. Han, S. Nam, T. Lim, S. Hong, H. Lee, J. Ind. Eng. Chem. 10 (2004) 302.
[26] T.X.T. Sayle, S.C. Parker, C.R.A. Catlow, Surf. Sci. 316 (1994) 329.
[27] H.C. Yao, Y.F.Y. Yao, J. Catal. 86 (1984) 254.
[28] F. Esch, S. Fabris, L. Zhou, T. Montini, C. Africh, P. Fornasiero, G. Comelli, R. Rosei, Science 309 (2005) 752.

[29] N. Laosiripojana, W. Sutthisripok, P. Kim-Lohsoontorn, S. Assabumrungrat, Int. J. Hydrogen Energy 35 (2010) 6747.
[30] R. Di Monte, J. Kašpar, Top. Catal. 28 (2004) 47.
[31] A. Hagemeyer, P. Trübenbach, C.W. Rieker, M. Wünsch, O. Watzernberger, EP Patent 0761594-A1, Assigned to BASF Aktiengesellschaft, 1997.
[32] A. Wolf, L. Mleczko, O.F. Schlüter, S. Schubert, WO2010133313-A1, Assigned to Bayer Material Science, 2010.
[33] G. Lee, S.W. Lee, I. Sohn, Y.C. Kwon, J. Song, C.-S. Son, WO2009035234-A2, Assigned to Hanwha Chemical Corporation, 2009.
[34] G. Dutta, U.V. Waghmare, T. Baidya, M.S. Hegde, K.R. Priolkar, P.R. Sarode, Chem. Mater. 18 (2006) 3249.
[35] G.R. Rao, B.G. Mishra, Bull. Catal. Soc. India 2 (2003) 122.
[36] H.A. Al-Madfaa, M.M. Khader, Mater. Chem. Phys. 86 (2004) 180.
[37] B.M. Reddy, P. Bharali, P. Saikia, J. Phys. Chem. C 112 (2008) 11729.
[38] F. Deganello, A. Martorana, J. Solid State Chem. 163 (2002) 527.
[39] A.P. Amrute, C. Mondelli, M.A.G. Hevia, J. Pérez-Ramírez, J. Phys. Chem. C 115 (2011) 1056.
[40] G. Kresse, J. Hafner, Phys. Rev. B 47 (1993) 558.
[41] J.-P. Perdew, K. Burke, M. Ernzerhof, Phys. Rev. Lett. 77 (1996) 3865.
[42] M. Cococcioni, S. Gironcoli, Phys. Rev. B 71 (2005) 035105.
[43] M.V. Ganduglia-Pirovano, J.L.F. Da Silva, J. Sauer, Phys. Rev. Lett. 102 (2009) 026101 (references therein).
[44] P.E. Blöchl, Phys. Rev. B 50 (1994) 17953.
[45] H.J. Monkhorst, J.D. Pack, Phys. Rev. B 13 (1976) 5188.
[46] G. Henkelman, B.P. Uberuaga, H. Jonsson, J. Chem. Phys. 113 (2000) 9901.
[47] D. Terribile, A. Trovarelli, C. de Leitenburg, G. Dolcetti, J. Llorca, Chem. Mater. 9 (1997) 2676.
[48] M.W.M. Hisham, S.W. Benson, J. Phys. Chem. 99 (1995) 6194.
[49] A.P. Amrute, C. Mondelli, M.A.G. Hevia, J. Pérez-Ramírez, ACS Catal. 1 (2011) 583.
[50] S. Tanuma, C.J. Powell, D.R. Penn, Surf. Interface Anal. 21 (1994) 165.
[51] D. Teschner, R. Farra, L.-D. Yao, R. Schlogl, H. Soerijanto, R. Schomaecker, T. Schmidt, L. Szentmiklósi, A.P. Amrute, C. Mondelli, J. Pérez-Ramírez, G. Novell-Leruth, N. Lopez, J. Catal. 285 (2012) 273.
[52] A. Badri, C. Binet, J. Lavalley, Faraday Trans. 92 (1996) 4669.
[53] A. Laachir, V. Perrichon, A. Badri, J. Lamotte, E. Catherine, J.C. Lavalley, J. El Fallah, L. Hilaire, F. Le Normand, E.E. Quéméré, G.N. Sauvion, O. Touret, Faraday Trans. 87 (1991) 1601.
[54] C. Binet, M. Daturi, J. Lavalley, Catal. Today 50 (1999) 207.
[55] T.B. Lindemer, J. Brynestad, J. Am. Ceram. Soc. 69 (1986) 867.
[56] J. Carrasco, N. Lopez, F. Illas, Phys. Rev. Lett. 93 (2004) 225502.
[57] J. Carrasco, F. Illas, N. Lopez, E.A. Kotomin, Y.F. Zhukovskii, R.A. Evarestov, Y.A. Mastrikov, S. Piskunov, J. Maier, Phys. Rev. B 73 (2006) 064106.
[58] P.M. Kowalski, M.F. Camellone, N.N. Nair, B. Meyer, D. Marx, Phys. Rev. Lett. 105 (2010) 146405.
[59] S. Chretien, H. Metiu, J. Phys. Chem. C 115 (2011) 4696.
[60] P.P. Dholabhai, J.B. Adams, P. Crozier, R. Sharma, J. Chem. Phys. 132 (2010) 094104.
[61] N. Lopez, J.D. Prades, F. Hernandez-Ramirez, J.R. Morante, J. Pan, S. Mathur, Phys. Chem. Chem. Phys. 12 (2010) 2401.
[62] X.G. Wang, A. Chaka, M. Scheffler, Phys. Rev. Lett. 84 (2000) 3650.
[63] D.A. McQuarrie, J.D. Simon, Molecular Thermodynamics, University Science Books, Sausalito, California, 1999.